Journal of Environmental Chemical Engineering 11 (2023) 109207

Contents lists available at ScienceDirect

Journal of Environmental Chemical Engineering

journal homepage: www.elsevier.com/locate/jece

Photoactivity of boron-or nitrogen-modified TiO_2 for organic pollutants degradation: Unveiling the photocatalytic mechanisms and by-products

Ailton.J. Moreira [a,b,*], Barbara R.M. dos Santos [c,d], Jeferson A. Dias [c], Pietra T. Rabello [a], Dyovani Coelho [a], Lucia H. Mascaro [a], Gian P.G. Freschi [b], Yara G. Gobato [a,b,c,d,e], Helder V.A. Galeti [a,b,c,d,e], Valmor R. Mastelaro [e], Ernesto Chaves Pereira [a,**]

[a] Universidade Federal de São Carlos, Zip Code 13565-905, São Carlos, SP, Brazil
[b] Universidade Federal de Alfenas, campus Poços de Caldas, Zip Code 37715-400, Poços de Caldas, MG, Brazil
[c] Institute of Science and Technology, Federal University of Lavras, ZIP Code: 37950-000, São Sebastião do Paraíso, MG, Brazil
[d] Department of Engineering, Federal University of Lavras, ZIP Code: 37200-000, Lavras, Minas Gerais, Brazil
[e] São Carlos Institute of Physics, University of São Paulo, PO Box 369, São Carlos 13560-970, SP, Brazil

ARTICLE INFO

Editor: Dr. G. Palmisano

Keywords:
Emerging pollutants. Intermediary levels. Photocatalysis. Degradation mechanism

ABSTRACT

The degradation of fluoxetine (FLX) emerging pollutant and the formation of by-products, potentially present in environmental ecosystems, was investigated from photocatalytic processes. Applying different synthesis methods, nitrogen (TiN) or boron (TiB)-modified TiO_2 presented oxygen vacancies (Vö) responsible for generating intermediate energy levels, which acted as shallow traps to minimize the recombination processes and maintain the efficient separation of charge carriers. All photocatalysts showed the potential to produce hydroxyl radicals ($^{\bullet}OH$) from the oxidation of water in h^+(VB), achieving 100% of RhB degradation under UV or visible irradiation. For the degradation of FLX, an alternative mechanism mediated by one of the by-products was confirmed after LC-MS-Q-TOF analysis. The protonation, dehalogenation and hydroxylation steps of FLX (m/z $[H^+]$ =310.1419) produce the transformation products TP8 ($m/z[H^+] = 310.1430$), TP6 ($m/z[H^+] = 286.1454$), and TP9 (m/z = 161.0221 (-ESI)), respectively. Other by-products have been identified after photodegradation, and their presence in FLX-contaminated ecosystems cannot be ignored. Therefore, high-performance photocatalysts obtained in this study are real alternatives for the environmental remediation of organic pollutants in aquatic ecosystems.

1. Introduction

In recent decades, the inappropriate discard of pesticides and pharmaceuticals has emerged as one of the biggest sources of environmental pollution with potential damage to the environment and public health [1–3]. The evident damage occurs because the conventional processes of water treatment and effluents are inefficient in degrading these compounds, classified as emerging contaminants [4,5]. Due to the potential risks of this new class of pollutants, the world scientific community has found, in semiconductor nanotechnology, efficient and sustainable processes for the environmental remediation of these compounds [6,7]. In this technology, nanostructured semiconductors can be activated by light to trigger a series of physicochemical processes that result in the production of reactive species capable of oxidizing pollutants in the reaction medium [8,9].

Titanium dioxide (TiO_2) is one of the most investigated semiconductors due to its diverse technological applications [10,11], especially for the degradation of emerging contaminants [12]. For this semiconductor, its uses are directed according to the crystalline structures that TiO_2 can assume, where the three main phases are rutile, anatase, and brookite, considered stable (rutile) and metastable (anatase and brookite) [13,14]. The metastable phases, especially anatase, are photoactive and widely used in water and effluent treatment processes by heterogeneous photocatalysis [15,16]. However, the high efficiency for environmental remediation depends on the capacity of the semiconductor to maintain the separation of charge carriers (h^+ - e^-) after the excitation of the e- from the valence band (VB) to the conduction band (CB) through the light source [17,18]. The anatase phase in its pure form

* Corresponding author at: Universidade Federal de São Carlos, Zip Code 13565-905, São Carlos, SP, Brazil.
** Corresponding author.
E-mail addresses: aijomoquim@gmail.com (Ailton.J. Moreira), ernesto@ufscar.br (E.C. Pereira).

https://doi.org/10.1016/j.jece.2022.109207
Received 29 October 2022; Received in revised form 2 December 2022; Accepted 20 December 2022
Available online 21 December 2022

has a bandgap energy (E_{gap}) of about 3.2 eV, allowing the absorption of light radiation with $\lambda < 389$ nm to be sufficient to promote the electron from VB to CB [19]. However, the charge carriers generated can recombine and make the semiconductor inefficient for photocatalytic applications. [20,21].

The addition of co-catalysts has been a great strategy to minimize the recombination processes in the TiO_2 structure, in addition to allowing its photoactivation with lower energy radiation, such as visible light [22, 23]. When added, co-catalysts can generate intermediate energy levels in the semiconductor band structure that act as shallow or deep traps for the excited e^-, preventing recombination [13,24]. Boron and nitrogen are two candidates for non-metallic co-catalysts that have shown great potential to obtain modified TiO_2 [25]. When inserted into the TiO_2 structure, they can generate intermediate energy states that increase the oxygen vacancies in the structure and, consequently, their ability to absorb visible light is improved [26]. Nonmetals can also occupy interstitial sites in the TiO_2 crystal structure in the form of NOx, BxHy, and BxOy species, which also contribute to minimizing recombination processes [26,27].

This increase in the potential for light absorption and the formation of color centers that minimize recombination are sufficient to maintain the flux of hole formation (h^+) in the VB [28,29]. The holes formed are the main responsible for promoting the oxidation of water to generate hydroxyl radicals ($^{\bullet}OH$) with the high oxidizing potential of organic pollutants [12,30]. However, in a recent review that deals with the photocatalytic activity of N-modified TiO_2, the proposed mechanisms are confronted, and many doubts are raised [25]. Among the main contradictions is the fact that even with the reduction of the bandgap of the modified TiO_2 and the proven formation of $^{\bullet}OH$, its efficiency for the degradation of some pollutants is not evidenced [25]. It is worth mentioning, however, that the literature has shown that the same photoactive material for a given pollutant is incipient in the presence of a pollutant of another chemical class [8,13]. This is because $^{\bullet}OH$ is non-selective, and its action depends on the chemical and kinetic nature of the reaction of the organic molecules that make up the reaction medium [31,32]. Briefly, in the photocatalytic step, $^{\bullet}OH$ can be directed to degrade by-products formed from the original pollutants, and, in these cases, the efficiency of removal of the original compound is impaired [33].

As the quantitative study of by-products is ignored in many photocatalysis studies, the authors cannot explain the inefficiency of the process even with the proven formation of $^{\bullet}OH$ [25]. However, this quantitative approach to the original pollutant and its transformation products (TP) has been addressed in recent studies [8,31]. Atrazine, FLX, and other compounds have shown that there is competition between the original pollutant and the by-products in the degradation mechanism, and this information should be considered [13,31]. FLX, also known as Prozac®, is a widely used antidepressant, and its improper disposal has resulted in environmental contamination of aquatic ecosystems. Furthermore, some by-products have shown greater environmental toxicity than the original pollutants, and further scientific discussion of the photocatalytic process based on the by-products is necessary [31]. Therefore, the present study approaches the obtaining of B-or-N modified TiO_2 from three synthesis methods. Its physicochemical characteristics were studied by different characterization techniques to explain its photocatalytic activity. In this step, two organic pollutants were selected to prove that the chemical nature of the molecule is an important parameter for understanding photocatalytic efficiency. Especially for the FLX emerging contaminant that was chosen in this study, a deep investigation of the degradation mechanisms was investigated. Thus, it was discussed that the original pollutant has its degradation efficiency conditioned to the degradation of one of the formed by-products.

2. Experimental

2.1. Nanoparticle synthesis

Details of the synthesis method for each material can be found in the Supplementary Information. Table 1 presents the nomenclatures used to identify each sample used in this work, where "Ti" is due to the metallic precursor used (TiO_2), "B" or "N" to the respective co-catalyst used in the sample (B for boron and N for nitrogen) and “PP”, “MW” and “US” refers to the polymeric precursor (PP), microwave-assisted hydrothermal (MW), and sonochemical (US) methods, respectively.

2.2. Characterization and photocatalytic assays

This information can be seen in Supplementary Information.

3. Results and discussion

3.1. Structural characterization

The XRD patterns are presented in Fig. 1. All the diffractograms were indexed to their respective crystallographic phases utilizing the crystallographic cards from the ICSD. The TiO_2 polymorphs anatase ($I4_1/amd$, ICSD # 242104 [34]), rutile ($P4_2/mnm$, ICSD n. 257864 [35]), and brookite ($Pbca$, ICDS n. 121631 [16]) were observed in the diffractograms. Only the peaks related to the TiO_2 polymorphs were seen for samples modified with nitrogen (Fig. 1a). This result indicated that this element was solubilized into the TiO_2 structure independently of the type of chemical synthesis used. On the other hand, samples modified with boron remained with residues of H_3BO_3 (Fig. 1b), which was used as the boron precursor (ICSD #61354) [36]. The oxygen anion (O^{2-}) has a similar size to the nitrogen anion (N^{3-}) in the crystalline structure, favoring the modification by substitution in the lattice, but it can also occur interstitially [37,38]. On the other hand, the B-modifying will form mainly the B^{3+} species, which are smaller and would probably be included interstitially into the structure, its permanence being dependent on other synthesis parameters [37]. Anyway, the insertion of N or B in the TiO_2 network will occur along with crystal defects generation for charge compensation.

The interstitial inclusions are more challenging and justify the partial efficacy of doping. Importantly, the peaks' intensities of H_3BO_3 are higher for TiB_PP and are visible for TiB_US. Nevertheless, they disappeared for TiB_MW, indicating that the synthesis method used impacts the efficacy of boron doping. The absence of boron acid, boron oxide, or hydroxide peaks in the XRD patterns of the TIB_MW sample indicates the inclusion of this element in the TiO_2 structure. While the PP method uses only temperature as the driving force to the crystallization, the combined use of temperature and alternative forms of energy, such as pressure, stimulates the boron doping more efficiently than in the US or MW methods [23,33].

Raman spectroscopy was employed for an in-depth analysis of the TiO_2 structure, and each phonon mode was characterized according to our previous works [13,40]. For the N-modified samples (Fig. 1c), only the phonon modes from anatase and rutile are seen. Therefore, this result confirms that the TiO_2 polymorphs are the ones generated in this system despite the method of synthesis used. Moreover, it also confirms that no N-containing residue nor N-based secondary phase remains in the samples after the completion of the synthesis. On the other hand, the

Table 1
Nomenclature of boron or nitrogen modified TiO_2 samples.

B-modified TiO_2		N-modified TiO_2	
1	TiB_MW	4	TiN_MW
2	TiB_PP	5	TiN_PP
3	TiB_US	6	TiN_US

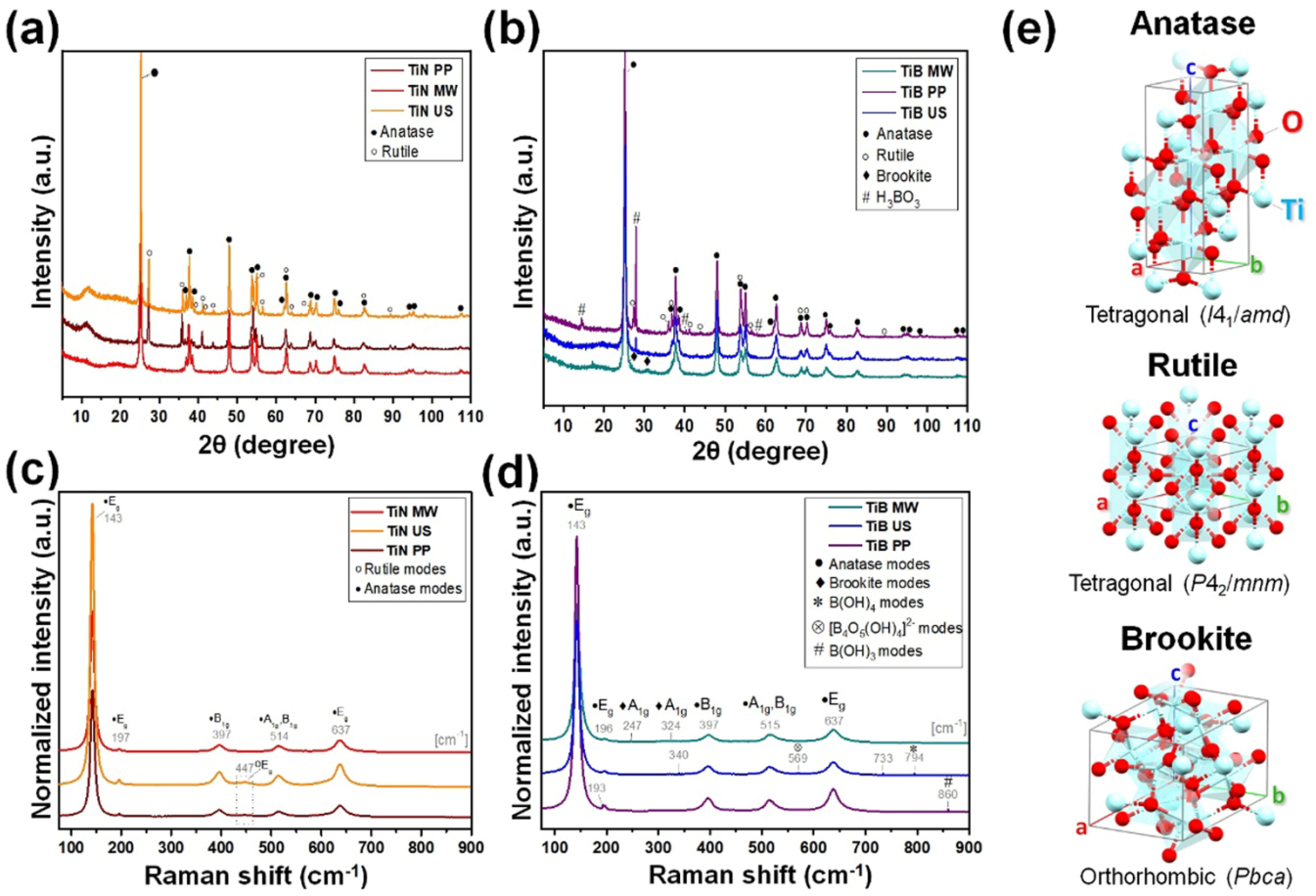

Fig. 1. XRD patterns of N-modified TiO_2 (a), B-modified TiO_2 (b), Raman spectra of N-modified TiO_2 (c), B-modified TiO_2 (d), and crystallographic representation of the TiO_2 polymorphs (e) by using the crystallographic information from Refs. [16,34,35,39].

results for B-modified materials confirm the presence of the remaining boric acid and other B-type hydroxides in the samples (Fig. 1d). Regarding the TiO_2 assignments, they presented mainly the phonon modes from the anatase polymorph, which is the dominant phase for these samples. Further, they also present modes of boron-based hydroxides that are seen only for the sample prepared by the US and PP methods but do not appear for the sample prepared by the MW method. These results are, therefore, in perfect agreement with the ones from XRD. They confirm that the B-doped sample prepared by the solvothermal-MW method is free of boron-based precursors, indicating the doping success. This sample has only characteristic modes of anatase and brookite polymorphs. On the other hand, the Raman spectroscopy showed TiB_PP and TiB_US presented bands of hydrated-boron phases at small intensity, which is not possible to see by X-ray Diffractometry due to the limitation of the technique.

Also, the low-intensity modes observed in Raman spectra are related not only to the H_3BO_3 precursor but also to other boron-type hydrated species such as $B(OH)_4^-$ and $[B_4O_5(OH)_4]_2^-$ [28,29]. In addition to the attributions presented, other phonon modes of very small intensity could be detected at 733, 340, and 193 cm^{-1}, which are also attributed to B_xH_y, B_xO_y, or $B_xO_yH_z$ species [41]. Regarding the TiO_2 polymorphism, the TiO_2 polymorph structures are represented in Fig. 1e. Importantly, the photoactive and metastable-anatase phase is the dominant polymorph in the diffractograms based on the relative intensities of the peaks and Raman spectra. The similarly photoactive and metastable-brookite phase also appears in TiB_MW in small quantity, while the poorly photoactive and the most stable phase (rutile) appears in moderate quantity for a series of the other samples [42]. Thus, Rietveld Refinement was used for quantitative analysis of the weight percentage (wt%) for each polymorph, and the results are presented in Table 2. Furthermore, the lattice parameters *a, b,* and *c* for each polymorph phase are presented as well, and the quality parameters obtained indicate convergence and adequate crystallographic indexation.

In a previous study, we applied the same synthesis methods to obtain pure TiO_2, and the influence of temperature and pressure, as well as the use of isopropanol, were reported as influencers of the phases formed [33]. In the current study, the use of N or B to modify TiO_2 showed that the presence of these elements was able to increase the amount of the metastable-anatase phase by up to 57%, compared to the pure TiO_2 reported in the previous study [33]. The crystalline structure of the pure samples presented in the previous study and the modified current samples confirmed differences in the phase composition. However, a special highlight is observed for the samples obtained by the PP method. For these, the presence of co-catalysts produced a semiconductor with only 36% (TiN_PP) or 6% (TiB_PP) of the rutile phase, while pure TiO_2 presented 93% of this same phase [33]. Even with the increase in obtaining the phase of interest (anatase), higher contents of the equilibrium phase, rutile, were obtained for TiN_PP and TiB_PP. The inducing of crystallization through solvothermal conditions or sonochemistry may increase the metastable phase generation due to the synergic effect of pressure and temperature [42,43]. Structurally, the samples presented a good concordance of the refined patterns to those crystallographic phases presented. This result confirms the adequate crystallinity of the prepared samples.

3.2. Surface characterization

XPS analyses were performed to characterize the surface of

Table 2
Lattice parameters for each TiO_2 polymorph and weight percentage (wt%) of the crystallographic phases in the samples obtained by Rietveld refinement analyses. The quality parameters goodness of fitting (χ^2) and the weighted profile R factor (R_{wp}) are presented as well.

Samples		*a, b* (Å)	*c* (Å)	^{V} (Å^3)	wt. (%)	Phases	$^{R}_{wp}$ (%)	$_{\chi}2$
N-doped TiO_2	TiN_PP	3.788 (1)	9.527 (6)	136.7	64	Anatase	11.87	1.18
		4.598 (2)	2.963 (2)	62.6	36	Rutile		
	TiN_MW	3.786 (1)	9.513 (4)	136.4	100	Anatase	14.66	1.70
	TiN_US	3.785 (7)	9.519 (3)	136.4	88	Anatase	10.77	1.36
		4.596 (2)	2.960 (2)	62.5	12	Rutile		
B-doped TiO_2	TiB_PP	3.786 (9)	9.518 (4)	136.4	71	Anatase	12.49	1.22
		4.542 (5)	2.958 (7)	60.0	6	Rutile		
		–	–	–	23	H_3BO_3		
	TiB_MW	3.786 (2)	9.505(9)	136.3	92	Anatase	13.75	1.41
		9.050 (1)[a]	5.124 (5)	261.8	8	Brookite		
	TiB_US	3.787(6)	9.514 (8)	136.4	95	Anatase	14.44	1.93
		–	–	–	5	H_3BO_3		

[a] For bookite, a ≠ b ≠ c. The value a is the one presented upward, while the refined b value is 5.643(7).

materials, and XPS survey spectra of TiN or TiB samples are shown in Fig. 2a - b. For TiN, the Ti (2 s, $2p_{3/2}$, 3 s, and 3p), C 1 s, and O 1 s core levels were observed, and the average amount of N for TiN samples was 0.23 at%. The same elements and core levels were also found in the XPS survey spectra of TiB samples. Also, the B 1 s core level was observed, confirming the presence of B in the TiB samples, with an average concentration of 0.13 at% [23,44]. To investigate the electronic structure of each element in detail, high-resolution XPS spectra were collected for B, N, Ti, and O (Figs. S1a and S1b). The Ti 2p core level presented two peaks centered at 465.0 and 459 eV, which are characteristic of the Ti^{4+} present in the Ti-O bond [40,45]. Any significant change in the peak position was not noticed for the studied materials. The O 1 s spectrum of TiN samples presents a high-intensity peak centered at 529.8 eV, whereas for TiB samples, O 1 s level was also identified by a peak centered around 530.4. In both cases, they were deconvoluted in three components, one centered at 529.9 eV, one at 530.9, and one at 532.1. The O 1 s component around 529.8 eV is due to O-Ti (TiN samples) and O-Ti/O-B (TiB) samples. According to the literature, the other two components of O 1 s spectra can be attributed to oxygen vacancies and/or chemisorbed oxygen [46]. These vacancies could be formed due to the insertion of B or N species in the TiO_2 structure in substitutional, interstitial, or superficial positions [47,48].

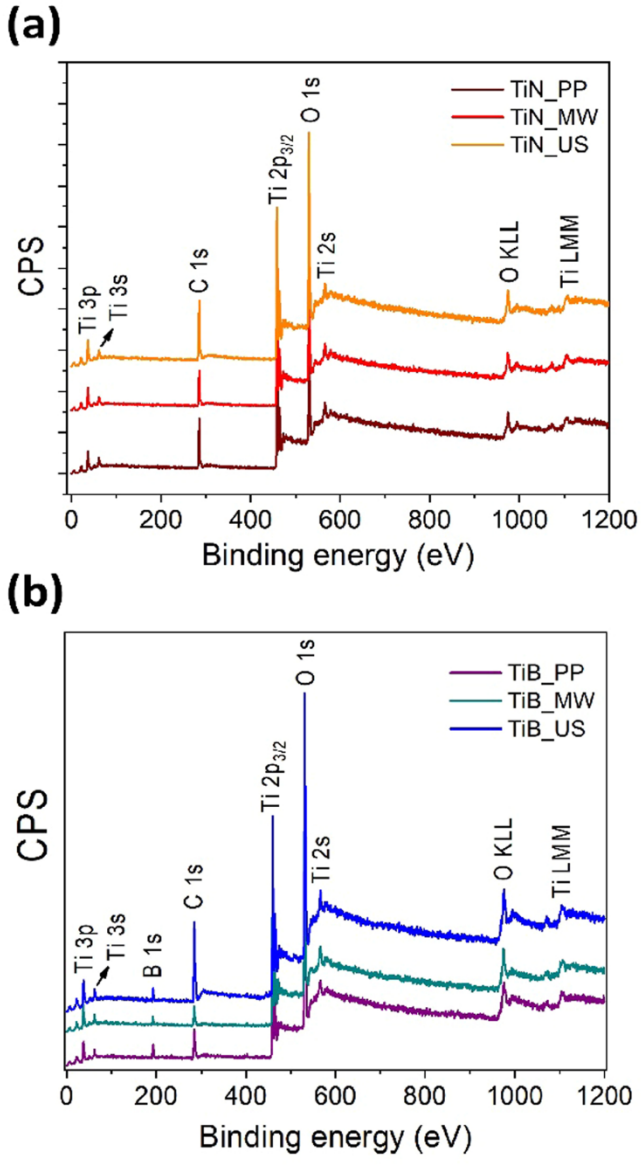

Fig. 2. XPS survey spectra of TiN (a) and TiB (b).

Fig. S1a shows the High-resolution N 1 s XPS spectra, confirming the presence of N-O bonds that represent the incorporation of N into the TiO_2 lattice at interstitial sites, oxygen vacancies, or on the surface [49–51]. For TiB (Fig. S1b), XPS results confirm the presence of B-O bounds for TiB_samples, the binding energy of 193.0 eV could be attributed to interstitial sites of TiO_2 lattice (B-O-Ti, called interstitial B, although the presence of B-O is also due the formation of H_3BO_3 detected by XRD results [41,52].

3.3. Morphological characterization

Fig. 3a-b showed that the TEM images of the TiN_MW and TiB_MW samples are formed by spherical nanoparticles with a mean size of 17.4 ± 7.5 nm or 12.9 ± 4.6 nm, respectively (Fig. 3c-d). The positive skewness of 0.67 and 1.11 calculated for TiB_MW and TiN_MW, respectively, confirms the heterogeneity of the nanoparticles and justifies the deviation of up to 43% found for the TiN_MW size. When the same method was applied to obtain pure TiO_2, spherical nanoparticles containing anatase and brookite with a size of 25 nm were formed [33]. As the standard deviation for TiN_MW was high, the sizes of TiN_MW and pure TiO_2 (25 nm) were statistically the same [33]. However, the modification with boron promotes a reduction in the particle size of up to 30%, considering the standard deviation of the measurement. The reduction noted for TiB_MW contributed positively to the stabilization of the brookite and anatase phases, which was found in higher quantities in all the samples [53]. This reduction can be attributed to the contracting capacity of the lattice in TiB_MW due to the presence of oxygen vacancies verified in the XPS analyses. TiB_PP, TiB_US, TiN_PP, and TiN_US showed a tendency to a spherical shape (Fig. S2), however, the size and count were not possible due to the greater agglomeration of these particles, which made it difficult to precisely define the contour regions.

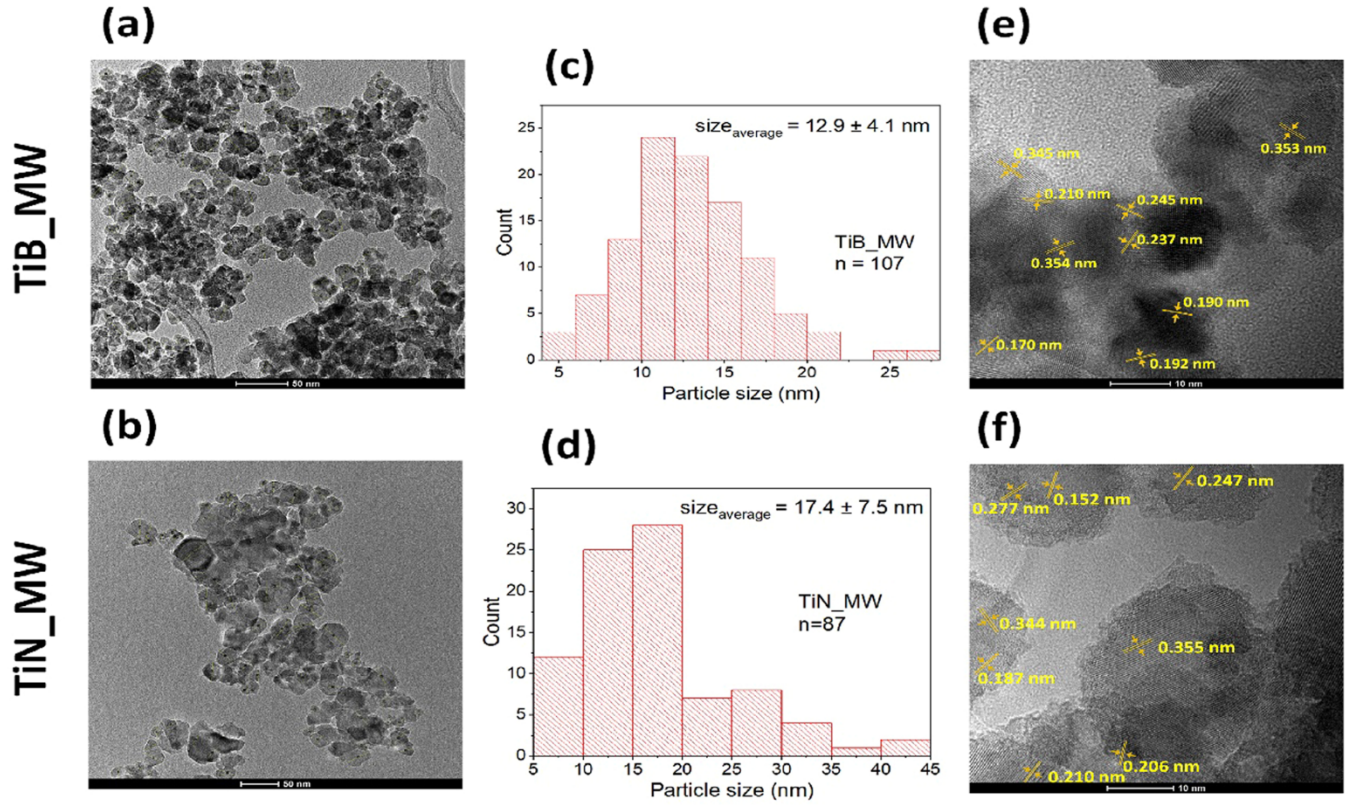

Fig. 3. TEM images (a-b), size distribution (c-d), and HR-TEM (e-f) of the TiB_MW and TiN_MW samples.

HR-TEM images obtained for TiB_MW and TiN_MW exhibited network fringes or D-spacing for both samples. The D-spacing distances were calculated by FFT analysis and its inverse in some network fringe domains, and the values are shown in Fig. 3e-f. Typical lattice fringes of anatase (0.170, 0.354, 0.355) and brookite (0.152, 0.210, 0.248, 0.277 and 0.344) were identified in TiB_MW and TiN_MW. Also, the lattice fringes (0.188, 0.190, 0.237, 0.245, 0.345) are present in some of the TiB_MW or TiN_MW samples that are confused between anatase and brookite. That is, although the XRD analysis for TiN_MW only demonstrates the presence of the anatase polymorph, small portions of brookite are possible to be present. This occurs because the most intense diffraction peak of anatase (related to the (101)-plane) overlaps the most intense peak of brookite (related to the (210)-plane). The presence of small portions of brookite is not expected to be detrimental to the photocatalytic performance of the material, since they present similar photocatalytic properties. Only a lattice fringe of 0.206 was found in the TiN_MW sample, which indicates that rutile is possible to be present in low quantity in this sample. That is, the absence of characteristic peaks and phonon modes from rutile in the XRD and Raman spectroscopy results, respectively, indicates that rutile is present at an exceptionally low quantity, under the detection limit from these techniques. So small quantity of rutile polymorph is not expected to be detrimental to the photocatalytic performance of the material as well.

3.4. Optical and electronic characterization

Once the presence of B and N in the structure of the materials and the contribution of different energy levels in the electronic movement for each element (Fig. 2) were confirmed, the diffuse reflectance and PL analyses were carried out to study the optical and electronic properties (Fig. 4). The band gap energies (E_{gap}) calculated by the Tauc plot equation (Fig. 4a-b) showed a shift towards the visible region compared to the pure materials presented in a previous study [33]. This shift is due to the energy levels attributed to Ti-O-N or N-O bonds of TiN. For TiN_US, the surface re.

The PL spectra show several peaks (Fig. 4c – d) which were associated with intermediate electronic transitions within the band structure of TiO_2 samples. The similarity of the energy profiles for TiB or TiN with seven peaks of PL emission indicates that B or N are responsible for inducing the formation of oxygen defects in the TiO_2 structure [54–56]. Outstandingly, the contribution of the peaks centered at 1.921, 1.931, 2.098 and 2.201 eV for the 1 and 50 mW powers of the excitation source, while an important reduction of PL intensity of the peaks centered at 1.855, 2.012 and 2.250 eV was noticed with the increase of laser power at 50 mW. This lower PL intensity confirms that the intermediate energy levels centered at 1.855, 2.012 and 2.250 eV store a limited amount of photoexcited electrons. On the other hand, the significant increase in the intensity of the emission peaks centered at 1.921, 1.931, 2.098 and 2.250 eV shows the highest concentration of these defects in the TiO_2 structure. The intermediate levels generated due to oxygen vacancies act as intermediate levels that ease the photon absorption, increasing the density of photogenerated electrons. As a practical consequence of this proximity, a more effective transfer of electrons is expected to promote reduction reactions in the CB and oxidation in the VB to maintain electron flow. As these defects are associated with $V_{\ddot{O}}$ [57,58], it was proven that N,B doping was effective to obtain materials with potential for photocatalytic applications in the UV-Vis region of the light spectrum. The PL spectrum of the pure TiO_2 samples produced by the same synthesis methods [33] and applying the same excitation conditions is shown in Fig. S3. The pure TiO_2 showed PL emission with broadband and greater intensity than that observed for the TiB or TiN. Especially for the pure TiO_2 excited with a power of 50 mW, the broadband profile confirms that the material presents many defects responsible for increasing the recombination processes of charge carriers. This characteristic can lead the pure samples to present a lower performance than the TiB or TiN in photocatalytic applications.

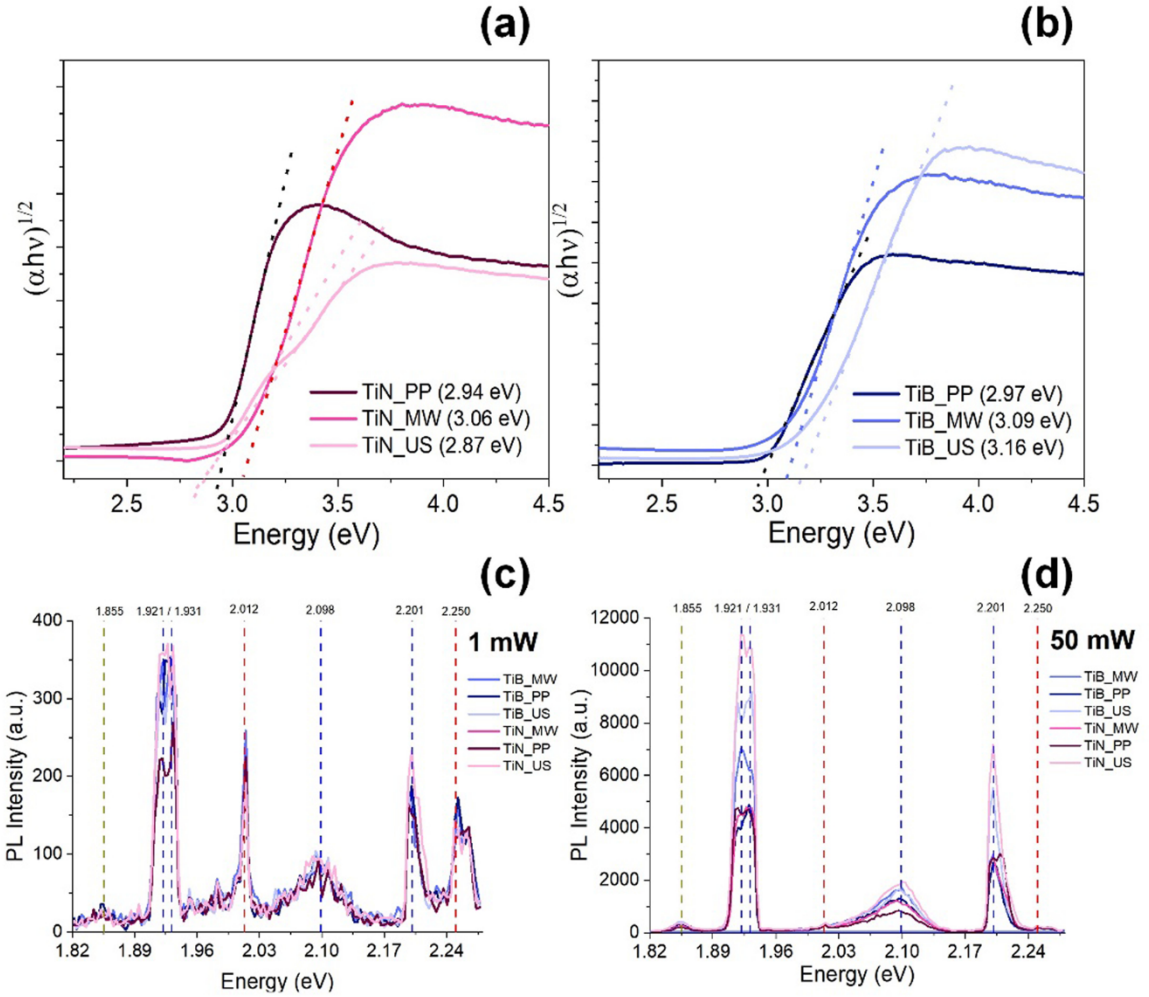

Fig. 4. Tauc plot of TiN(a) and TiB(b), Typical PL spectra for different TiO_2 samples for a laser excitation with a wavelength of 405 nm (3. 06 eV) and laser power of 1 mW(c) and 50 mW(d) at 300 K.

3.5. Photocatalytic activity

3.5.1. RhB photocatalysis

As the E_{gap} values calculated for the nanomaterials are located in the transient region of UV_Vis radiation (~ 2.9 – 3.2 eV), the photocatalytic activity under UV or Vis light was initially evaluated from the degradation of RhB (5 mg L^{-1}). Compared to photolytic reaction, photocatalysis of RhB under UV light exhibited high performance for TiN and TiB materials (Fig. 5a – b). Photolysis removed 28% of RhB within 60 min, while photocatalysis in the presence of TiN_MW and TiN_US removed > 95% in the same time (Fig. 5a). However, the most expressive results were the removal of 99% of RhB in just 15 min in the presence of B-modified TiO_2 (Fig. 5b). It is worth remembering that the TiB samples showed the highest amounts of $V_{\ddot{O}}$, as proved by the XPS analysis. Degradation results under visible light also confirmed that TiN or TiB materials actively respond to stimulus from this light source (Fig. 5c – d). This occurs because the electrons photogenerated by the lower energy (visible) radiation can be retained in the intermediate levels, as identified by the PL analysis (Fig. 4). These, in turn, act as shallow traps, and in the presence of the organic pollutant (RhB), the oxidation reactions in the VB feed the flow of charges in the electronic mechanism. Thus, the initially trapped electrons are conducted more efficiently to the CB due to its proximity to the intermediate levels. The RhB degradation under UV or visible light was also confronted by the reactions with the pure materials (Fig. S4). The RhB removal values applying the unmodified materials were lower than those obtained for the modified materials. These results confirm that modifications with nitrogen or boron were essential to producing materials with improved photocatalytic activity.

The maximum RhB removal (%) for all processes is shown in Fig. 5e. Under UV light, photocatalysis was superior to photolysis, showing that this excitation source is efficient to promote the processes of electronic transition and separation of charge carriers in all synthesized materials. The B-modified TiO_2 samples showed greater photoactivity compared to the N-modified TiO_2 samples. Still, when considering the synthesis methods, the TiB_MW and TiN_MW obtained by microwave-assisted hydrothermal method showed better results compared to the US or PP methods, especially under visible light. For these two materials, it is worth mentioning that the microwave-assisted hydrothermal method was the most efficient in producing the largest amount of the metastable and photoactive phases of TiO_2 (anatase and brookite). Furthermore, the highest BET area values, 67.0 m^2 g^{-1} for TiB_MW and 28.0 m^2 g^{-1} for TiN_MW were obtained using this method. The first-order kinetic constants were calculated and are shown in Table 3.

To unravel the main photocatalytic mechanisms mediated by TiN_MW and TiB_MW, the reagents TBA, EDTA, and SN were added to the dye solution as scavengers of $^{\bullet}OH$, h^{+}, and e^{-}, respectively [59,60], and the mixture was irradiated for 60 min Fig. 5f shows that SN has no inhibitory action in RhB degradation under UV or Vis light, except for TiB_MW(Vis) which shows a slight decrease in removal efficiency. In the presence of EDTA, all processes were affected, achieving inhibition of up to 56% compared to conventional photocatalysis. However, in the

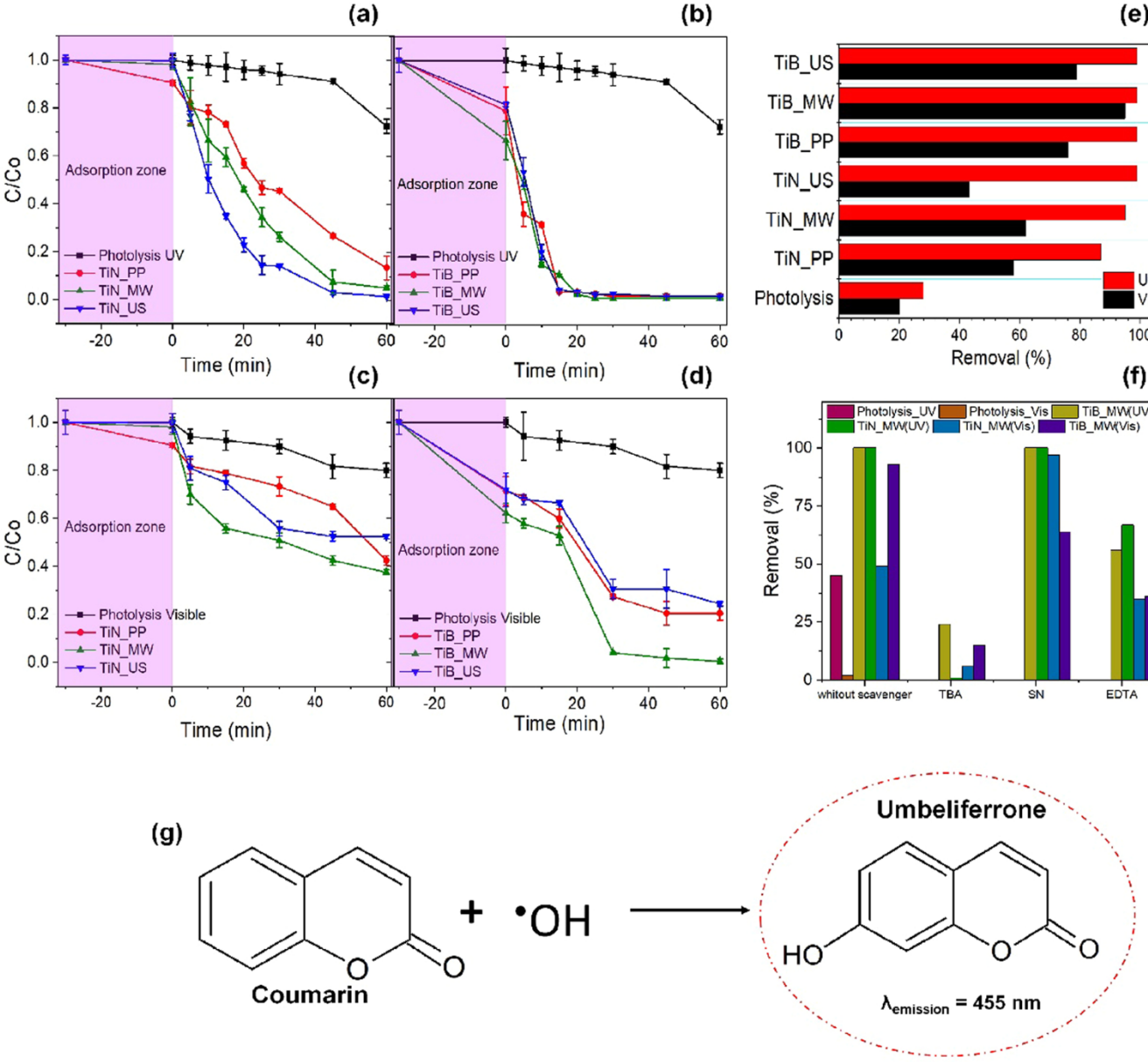

Fig. 5. RhB degradation curve in the presence of TiN(a), TiB(b) under ultraviolet light and TiN(c), TiB(d) under visible light. Removal (%) of RhB under different conditions and fixed time of 60 min (e), study with scavengers (f), and hydroxylation of coumarin (g).

Table 3
Values of kinetic constant (k = min^{-1}) and linear correlation coefficient (R^2) for each process of RhB degradation.

Photocatalyst	Visible		Ultraviolet	
	k x10^{-3} (min^{-1})	R^2	k x10^{-3} (min^{-1})	R^2
Photolysis	3.5 ± 0.4	0.9329	4.5 ± 1	0.7373
Ti_MW	18.4 ± 0.01	0.928	65.2 ± 0.01	0.927
TiN_PP	9.40 ± 2	0.7618	31.8 ± 2	0.9668
TiN_MW	11.6 ± 2	0.9585	54.0 ± 3	0.9702
TiN_US	9.7 ± 2	0.8562	75.0 ± 2	0.9898
TiB_PP	24.6 ± 4	0.8892	171 ± 35	0.9352
TiB_MW	88.7 ± 10	0.9386	160 ± 20	0.9395
TiB_US	19.8 ± 3	0.8677	176 ± 22	0.8464

presence of TBA, dye removal was inhibited by almost 100% for TiB_MW (UV) and by more than 75% for the other processes. Therefore, the degradation mechanisms mediated by e^- (CB) are not significant, while those mediated by h^+ and •OH were evidenced. The photocatalytic mechanisms mediated by h^+ and •OH are directly correlated since the •OH production occurs from the oxidation of water in h^+ (VB). The •OH -mediated mechanism is efficient due to the intermediate levels generated by $V_{\ddot{O}}$ since by inhibiting recombination, the separation of charge carriers promotes the continuous transfer of photoexcited electrons between the VB and CB. As a way of proving the •OH formation, probe assays with coumarin were carried out in the presence of all materials. According to the reaction represented in Fig. 5g, the •OH presence converts coumarin to its hydroxylated species (umbelliferone) which exhibits a PL emission peak centered at 455 nm when excited with a light source of 332 nm [9,23].

The PL spectra show that under UV light all materials are efficient to produce •OH (Fig. S5), which explains the high efficiency observed in dye removal. Under visible light, TiN_PP showed the poorest performance, which is explained by the lower capacity to produce •OH. Therefore, TiB_MW was shown to be active by different photocatalytic mechanisms, with emphasis on the •OH efficient production, revealing

the contribution of each mechanism and the influence of $V_{\ddot{O}}$ on the efficient removal of the dye. Fig. 6 and the equations from 1 to 4 present a proposal for a photocatalytic mechanism using TiB_MW as a model.

$$TiB\_MW(V_{\ddot{O}}) + hv \rightarrow h^+(VB) + e^-(CB) \quad (1)$$

$$h^+(VB) + H_2O \rightarrow {}^{\bullet}OH + e^- + H^+ \quad (2)$$

$$e^-(CB) + V_{\ddot{O}} \rightarrow V_O^{\circ} \quad (3)$$

$${}^{\bullet}OH + H^+ + RhB \rightarrow byproducts \quad (4)$$

Table 4 shows comparative data found in the current literature for the photocatalytic degradation of RhB under visible light. The results show that TiB_MW really has high performance.

3.5.2. FLX photocatalysis

For presenting the highest amounts of the (photoactive) anatase phase, high surface area, efficiency in generating $^{\bullet}OH$, and outstanding performance in studies with RhB under UV and Vis light, the photocatalysts TiN_MW and TiB_MW were selected for photocatalysis of FLX. Under visible light, the FLX degradation was at most 12% for photolysis, 41% for TiN_MW and 54% for TiB_MW in 60 min (Fig. 7). This increase in FLX degradation efficiency of up to 42% confirms the outstanding photoactivity of TiB_MW when exposed to the visible light source. However, the degradation limited to 54% is due to the high stability of this molecule. In a study developed by Kwon and Armbrust, 2006, the photochemical degradability of FLX was neglected due to low efficiency for 100 days of exposure to simulated sunlight [67].

Under UV light irradiation, FLX removal was > 90% for photolysis and TiN_MW, while TiB_MW could promote efficient degradation within up to 15 min of irradiation. However, it is worth noting that photocatalysis mediated by TiN_MW or TiB_MW was ~5% or ~12% superior to photolysis in the initial 5- or 10-min time, respectively, showing no significant improvement after 15 min. Given these results, it is noteworthy that both materials are efficient in producing $^{\bullet}OH$, especially when excited by UV light (Fig. S5). The literature shows that the degradation of FLX mediated by photolysis or $^{\bullet}OH$ is accompanied by the formation of different TP from the first moment of degradation [31]. Once formed, these by-products are oxidized by the $^{\bullet}OH$ produced in the photocatalytic mechanism and, consequently, compete with FLX, harming its degradation. [8,31]. Therefore, the smaller removal of FLX after the first degradation times does not characterize the inefficiency of the photocatalyst but exposes its potential to promote the degradation of other compounds formed from the degradation of FLX through an alternative photocatalytic mechanism, as already reported in other studies [31].

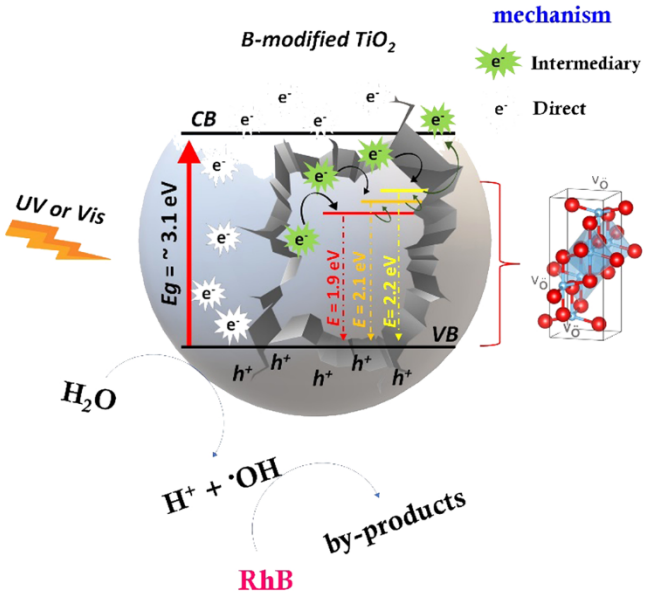

Fig. 6. Proposal of a TiB_MW-mediated photocatalytic mechanism for RhB degradation.

Table 4
Comparative data of photocatalytic degradation of RhB under visible light using different photocatalysts.

Photocatalyst	Solution volume (mL) / catalyst dosage (g/L) / RhB concentration (mg L^{-1})	Maximum removal (%) / Time (min)	Reference
CQDs/Sb_2WO_6	100 / 1 /10	99 / 120	[61]
$BiVO_4$-Ni/$AgVO_3$	50 / 0.6 / 10	99 / 30	[62]
Ti_3C_2Tx MXene (TCM) with Ag+ íons	30 / 0.3 / 20	100 / 120	[63]
g-C_3N_4/Ag/ZnO	50 / 1 / 10	~ 72 / 210	[64]
TiO2 (P25)	50 / 0.5 / 5	~ 70 / 60	[65]
TiO2 (P25)	100 / 1 / 8	40 / 80	[66]
TiN_MW	10 / 1 / 5	63 / 60	This work
TiB_MW	10 / 1 / 5	96 / 30	

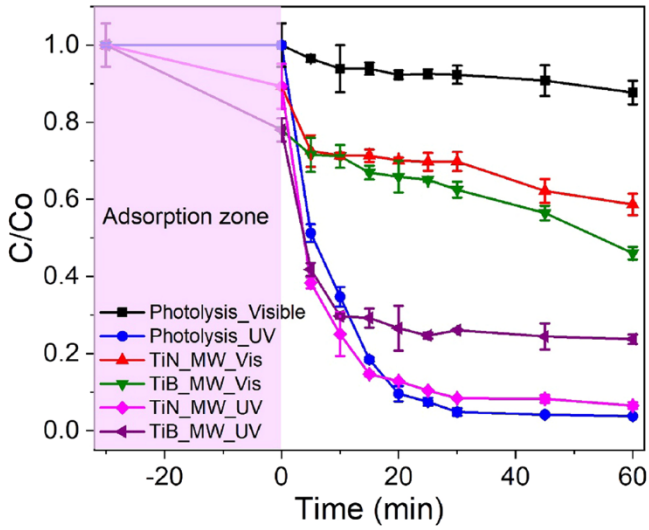

Fig. 7. FLX degradation curve mediated by different photochemistry processes.

To explore these alternative mechanisms, Fig. S6 and Fig. S7 / Table S1 show the chromatograms and $m/z[H^+]$ fragments obtained after LC-MS-Q-TOF analysis in scan mode (+) of FLX samples (standard), photolysis, and photocatalysis with TiN_MW or TiB_MW under UV light for 60 min, respectively. Fig. S6a, which refers to the undegraded FLX standard solution, identified a single peak at 5.31 min which was named TP9 with fragment $m/z[H^+] = 310.1418$. After 60 min photolysis (Fig. S6b), the degradation of TP9 was accompanied by the formation of TP1, TP4, TP5, TP6, TP7, and especially, TP8, which was shown to be the main degradation by-product of TP9 via photolysis. For the photocatalytic process with TiN_MW (Fig. S6c) and TiB_MW (Fig. S6d), the degradation of TP9 was not accompanied by the preferential formation of TP8, which reached a peak intensity comparable to TP6. These results show that for the photocatalytic processes, TP8 may be degraded with greater efficiency compared to photolysis. In addition, TP2 and TP3 were formed in greater amounts in the degradation process mediated by TiB_MW.

The $m/z[H+]$ fragments (Fig. S7) were used to propose the molecular structure of each by-product. As TP8 is formed in large amounts by photolysis and was found in the photocatalytic reaction medium, the mechanism of TP9 protonation was suggested. This light-activated mechanism justifies the presence of TP8 in all samples and

corroborates the compatibility of the fragments $m/z[+] = 310.1423$ and $m/z[H^+] = 310.1425$ that were assigned to TP8 and TP9, respectively. The protonated species of TP9 in the acidic range of the pH have already been reported in a previous study [68]. Likewise, the decrease in pH of TP9 photodegraded solutions has also been reported [32,69], which makes the proposal of the protonated structure for TP8 consistent. Therefore, the higher amount of TP8 in the photolytic system shows that the protonation of TP9 increases the persistence of the formed by-product. However, in the presence of TiN_MW or TiB_MW, the $^{\bullet}OH$ formed by the photocatalytic mechanism oxidizes TP8 more efficiently, which explains its lower amount in these systems. Detailing the reaction mechanism, hydroxylation of the $-CF_3$ group and deprotonation of the amine group of TP8 to form a carboxylated structure can be mediated by hydrolysis or $^{\bullet}OH$ attack, giving rise to TP6. This, in turn, can undergo demethylation of the amine group, also mediated by $^{\bullet}OH$, to give rise to TP7.

In addition to these main mechanisms, TP4 and TP5 are also produced by the TP8 hydroxylation mechanism. The TP4 compound is formed after the removal of the aromatic ring positioned on the chiral carbon, hydroxylation at different positions of the carbon chain, and mono-dehalogenation of the $-CF_3$ group originally present in TP8. TP5, on the other hand, is the result of demethylation of the amine group and hydroxylation of the carbon neighboring the amine to form an amide group due to the deprotonation of the hydroxyl group. The highest amounts of TP2 and TP3 were noted for the TiB_MW process, showing that this mechanism mediated by breaking the ether bond of TP8 can give rise to TP1 + TP2 or TP3 + TP2. Therefore, as shown in the RhB degradation steps, the photocatalytic degradation processes presented for FLX removal are also mediated by the $^{\bullet}OH$ formed by the exposure of photocatalysts to UV light. For clarity, Eqs. 5 to 10 and Fig. 8 present a proposal for the TP9 degradation mechanism. The arrow and blue highlight indicate a preferential mechanism mediated by photolysis, while the arrow and red highlight follow a preferential mechanism mediated by photocatalysis with TiB_MW. The other mechanisms are observed for both degradation processes.

$$TP9 + H_2O + hv \rightarrow TP8 + OH^- \quad (5)$$

$$TiB\_MW + hv \rightarrow h^+(VB) + e^-(CB) \quad (6)$$

$$h^+(VB) + OH^- \rightarrow {}^{\bullet}OH + e^-(CB) \quad (7)$$

$$e^-(CB) + V_{\ddot{O}} \rightarrow V_O^{\circ} \quad (8)$$

$$TP8 + {}^{\bullet}OH \rightarrow \text{by-products (main mechanism)} \quad (9)$$

$$TP9 + {}^{\bullet}OH \rightarrow \text{by-products (secondary mechanism)} \quad (10)$$

This proposed mechanism that shows greater potential for materials to degrade TP8 instead of TP9 can also be attributed to the electrostatic interaction between the photocatalyst and TP8. As shown in Fig. 1e, the oxygen sites of the anatase crystal structure have greater surface exposure, and together with the N or B co-catalysts obtain a more negative character. Thus, the protonated structure of TP8 potentiates the electrostatic photocatalyst-molecule interaction to promote efficient degradation. As $^{\bullet}OH$ is primarily responsible for oxidation reactions, Fig. 9 illustrates the photocatalytic degradation mechanism of FLX to form the main by-products.

4. Conclusion

The photocatalysts synthesized in this work are versatile for efficiently producing $^{\bullet}OH$ under UV or visible light, and photodegrading organic pollutants by different mechanisms. By unraveling the by-products formed in the FLX degradation step, important information about the presence of potential new molecules in environmental ecosystems is provided in this study. It has been shown in detail that an efficient photocatalyst for the degradation of a given class of organic pollutants may not show the same photocatalytic response for another class. However, this behavior does not indicate that the photocatalyst is inefficient, only that it can act by a different degradation mechanism in which the by-product, when formed, limits the degradation of the original pollutant. These strong indications of competition in

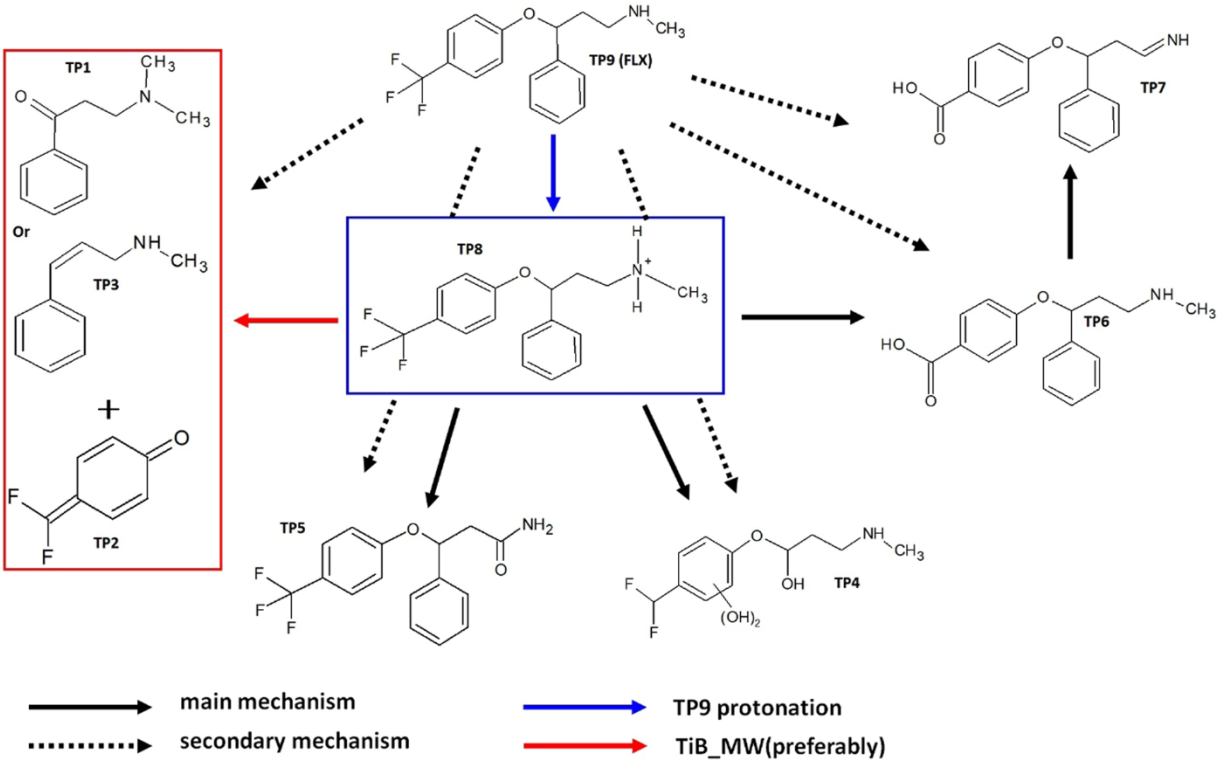

Fig. 8. Proposed mechanism of FLX degradation after photolytic or photocatalytic degradation using as a basis the m/z fragments obtained by LC-MS-Q-TOF analysis.

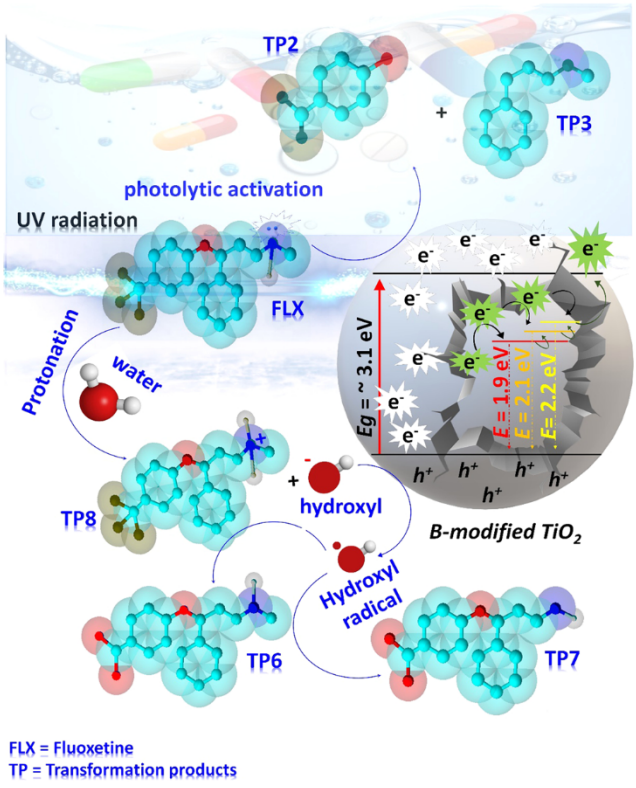

Fig. 9. Illustrative image of the mechanisms involved in the formation of the main by-products.

degradation mechanisms should be taken into account in future research.

CRediT authorship contribution statement

Ailton J Moreira: Writing - original draft and methodology. **Barbara R.M dos Santos:** Methodology, Writing (structural properties). **Jeferson A. Dias:** Review & editing (structural properties). **Pietra T. Rabello:** Methodology (Photocatalysis). **Dyovani Coelho:** review & editing (Structural and morphological properties). **Lucia H. Mascaro:** Review & editing. **Gian Paulo Giovanni Freschi:** Review & editing. **Yara G. Gobato:** Methodology, Writing - review (optical properties); **Helder V.A. Galeti:** Methodology, Writing - Editing (optical properties); **Valmor R. Mastelaro:** Methodology, Writing - Review & editing (XPS analysis). **Ernesto C. Pereira:** Supervision, writing - review & editing.

Declaration of Competing Interest

The authors declare that they have no known competing financial interests or personal relationships that could have appeared to influence the work reported in this paper.

Data availability

Data will be made available on request.

Acknowledgments

The authors would like to thank the Fundação de Amparo a Pesquisa do Estado de Minas Gerais (Grant: APQ-00601-22), Coordenação de Aperfeiçoamento de Pessoal de Nível Superior (CAPES) and Fundação de Amparo à Pesquisa do Estado de São Paulo (grants: 2013/07296-2, 2016/20609-8, 2017/11986-5), Conselho Nacional de Desenvolvimento Científco e Tecnológico [CNPq (PIBIC UFLA grant #PIICT177-2021 for the fellowship of B.R.M. Santos)], and Shell is gratefully acknowledged.

Appendix A. Supporting information

Supplementary data associated with this article can be found in the online version at doi:10.1016/j.jece.2022.109207.

References

[1] F. Desbiolles, L. Malleret, C. Tiliacos, P. Wong-Wah-Chung, I. Laffont-Schwob, Occurrence and ecotoxicological assessment of pharmaceuticals: is there a risk for the Mediterranean aquatic environment, Sci. Total Environ. 639 (2018) 1334–1348, https://doi.org/10.1016/j.scitotenv.2018.04.351.
[2] I.L. Costa, A.L. Pletsch, Y.R. Torres, Occurrence of antidepressant drugs in the environment - a review, Rev. Virtual Quim. 6 (2014) 1408–1431, https://doi.org/10.5935/1984-6835.20140092.
[3] A.B. Cundy, F.M. Rowlands, G. Lu, W.-X. Wang, A systematic review of emerging contaminants in the Greater Bay Area (GBA), China: current baselines, knowledge gaps, and research and management priorities, Environ. Sci. Policy 131 (2022) 196–208, https://doi.org/10.1016/j.envsci.2022.02.002.
[4] C.M. Lee, P. Palaniandy, I. Dahlan, Pharmaceutical residues in aquatic environment and water remediation by TiO2 heterogeneous photocatalysis: a review, Environ. Earth Sci. 76 (2017), https://doi.org/10.1007/s12665-017-6924-y.
[5] H. He, Y. Liu, S. You, J. Liu, H. Xiao, Z. Tu, A review on recent treatment technology for herbicide atrazine in contaminated environment, Int. J. Environ. Res. Public Health 16 (2019), https://doi.org/10.3390/ijerph16245129.
[6] M.K. Shahid, A. Kashif, A. Fuwad, Y. Choi, Current advances in treatment technologies for removal of emerging contaminants from water – a critical review, Coord. Chem. Rev. 442 (2021), 213993, https://doi.org/10.1016/j.ccr.2021.213993.
[7] M. Dubey, S. Mohapatra, V.K. Tyagi, S. Suthar, A.A. Kazmi, Occurrence, fate, and persistence of emerging micropollutants in sewage sludge treatment, Environ. Pollut. 273 (2021), 116515, https://doi.org/10.1016/j.envpol.2021.116515.
[8] E.T. Jesus, A.J. Moreira, M.C. Sá, G.P.G. Freschi, M.R. Joya, M.S. Li, E.C. Paris, Potential of Nb2O5 nanofibers in photocatalytic degradation of organic pollutants, Environ. Sci. Pollut. Res. 28 (2021) 69401–69415, https://doi.org/10.1007/s11356-021-15435-8.
[9] E.C. Paris, J.O.D. Malafatti, A.J. Moreira, L.C. Santos, C.R. Sciena, A. Zenatti, M. T. Escote, V.R. Mastelaro, M.R. Joya, CuO nanoparticles decorated on hydroxyapatite/ferrite magnetic support: photocatalysis, cytotoxicity, and antimicrobial response, Environ. Sci. Pollut. Res. 29 (2022) 41505–41519, https://doi.org/10.1007/s11356-021-18263-y.
[10] M. Manzoli, F.S. Freyria, N. Blangetti, B. Bonelli, Brookite, a sometimes under evaluated TiO2polymorph, RSC Adv. 12 (2022) 3322–3334, https://doi.org/10.1039/d1ra09057g.
[11] B.S. Pinheiro, L.L. Gimenes, A.J. Moreira, A.F. de Araújo, C.D. Freschi, G.P. G. Freschi, Speciation of As in environmental samples using the nano-TiO2/PCHG-FAAS online system, J. Environ. Sci. Heal. - Part A Toxic. /Hazard. Subst. Environ. Eng. 52 (2017) 1089–1098, https://doi.org/10.1080/10934529.2017.1340749.
[12] S.J. Mazivila, I.A. Ricardo, J.M.M. Leitão, J.C.G. Esteves da Silva, A review on advanced oxidation processes: From classical to new perspectives coupled to two- and multi-way calibration strategies to monitor degradation of contaminants in environmental samples, Trends Environ. Anal. Chem. 24 (2019) 1–10, https://doi.org/10.1016/j.teac.2019.e00072.
[13] A.J. Moreira, D. Coelho, J.A. Dias, L.H. Mascaro, G.P.G. Freschi, V.R. Mastelaro, E. C. Pereira, Phase control and optimization of photocatalytical properties of samarium doped TiO2 synthesized by coupled ultraviolet and microwave radiations, J. Alloy. Compd. 905 (2022), 164217, https://doi.org/10.1016/j.jallcom.2022.164217.
[14] D. Dambournet, I. Belharouak, K. Amine, Tailored preparation methods of TiO2 anatase, rutile, brookite: Mechanism of formation and electrochemical properties, Chem. Mater. 22 (2010) 1173–1179, https://doi.org/10.1021/cm902613h.
[15] J.H. Leal, Y. Cantu, D.F. Gonzalez, J.G. Parsons, Brookite and anatase nanomaterial polymorphs of TiO2 synthesized from TiCl3, Inorg. Chem. Commun. 84 (2017) 28–32, https://doi.org/10.1016/j.inoche.2017.07.014.
[16] H.Y. Playford, Variations in the local structure of nano-sized anatase TiO2, J. Solid State Chem. 288 (2020), 121414, https://doi.org/10.1016/J.JSSC.2020.121414.
[17] J.J.M. Vequizo, H. Matsunaga, T. Ishiku, S. Kamimura, T. Ohno, A. Yamakata, Trapping-Induced enhancement of photocatalytic activity on brookite TiO 2 powders: comparison with anatase and rutile TiO 2 powders, ACS Catal. 7 (2017) 2644–2651, https://doi.org/10.1021/acscatal.7b00131.
[18] S.M. El-Sheikh, T.M. Khedr, A. Hakki, A.A. Ismail, W.A. Badawy, D.W. Bahnemann, Visible light activated carbon and nitrogen co-doped mesoporous TiO2 as efficient photocatalyst for degradation of ibuprofen, Sep. Purif. Technol. 173 (2017) 258–268, https://doi.org/10.1016/j.seppur.2016.09.034.
[19] A.N. Kadam, R.S. Dhabbe, M.R. Kokate, Y.B. Gaikwad, K.M. Garadkar, Preparation of N doped TiO2 via microwave-assisted method and its photocatalytic activity for degradation of Malathion, Spectrochim. Acta - Part A Mol. Biomol. Spectrosc. 133 (2014) 669–676, https://doi.org/10.1016/j.saa.2014.06.020.
[20] A. Yamakata, J.J.M. Vequizo, Curious behaviors of photogenerated electrons and holes at the defects on anatase, rutile, and brookite TiO2 powders: a review,

J. Photochem. Photobiol. C Photochem. Rev. 40 (2019) 234–243, https://doi.org/10.1016/j.jphotochemrev.2018.12.001.
[21] G. Botelho, J.C. Sczancoski, J. Andres, L. Gracia, E. Longo, Experimental and theoretical study on the structure, optical properties, and growth of metallic silver nanostructures in Ag3PO4, J. Phys. Chem. C 119 (2015) 6293–6306, https://doi.org/10.1021/jp512111v.
[22] C. Carlucci, B.F. Scremin, T. Sibillano, C. Giannini, E. Filippo, P. Perulli, A. L. Capodilupo, G.A. Corrente, G. Ciccarella, Microwave-assisted synthesis of boron-modified TiO 2 nanocrystals, Inorganics 2 (2014) 264–277, https://doi.org/10.3390/inorganics2020264.
[23] A.J. Moreira, J.O.D. Malafatti, T.R. Giraldi, E.C. Paris, E.C. Pereira, V.R. de Mendonça, V.R. Mastelaro, G.P.G. Freschi, Prozac® photodegradation mediated by Mn-doped TiO<inf>2</inf> nanoparticles: evaluation of by-products and mechanisms proposal, J. Environ. Chem. Eng. 8 (2020), https://doi.org/10.1016/j.jece.2020.104543.
[24] M.A. Moyet, R.B. Arthur, E.E. Lueders, W.P. Breeding, H.H. Patterson, The role of Copper (II) ions in Cu-BiOCl for use in the photocatalytic degradation of atrazine, J. Environ. Chem. Eng. 6 (2018) 5595–5601, https://doi.org/10.1016/j.jece.2018.08.057.
[25] J.A. Rengifo-Herrera, P. Osorio-Vargas, C. Pulgarin, A critical review on N-modified TiO2 limits to treat chemical and biological contaminants in water. Evidence that enhanced visible light absorption does not lead to higher degradation rates under whole solar light, J. Hazard. Mater. 425 (2022), https://doi.org/10.1016/j.jhazmat.2021.127979.
[26] D. Wu, J. Guo, H. Wang, X. Zhang, Y. Yang, C. Yang, Z. Gao, Z. Wang, K. Jiang, Green synthesis of boron and nitrogen co-doped TiO2 with rich B-N motifs as Lewis acid-base couples for the effective artificial CO_2 photoreduction under simulated sunlight, J. Colloid Interface Sci. 585 (2021) 95–107, https://doi.org/10.1016/j.jcis.2020.11.075.
[27] K. Ma, M. Zhang, W. Sun, C. Dong, Y. Dong, W. Hao, Y. Ding, Revealing different depth boron substitution on interfacial charge transfer in TiO2 for enhanced visible-light H2 production, Appl. Catal. B Environ. 315 (2022), 121570, https://doi.org/10.1016/j.apcatb.2022.121570.
[28] J.M. Herrmann, Heterogeneous photocatalysis: fundamentals and applications to the removal of various types of aqueous pollutants, Catal. Today 53 (1999) 115–129, https://doi.org/10.1016/S0920-5861(99)00107-8.
[29] K.C. Christoforidis, M. Fernández-García, Photoactivity and charge trapping sites in copper and vanadium doped anatase TiO2 nano-materials, Catal. Sci. Technol. 6 (2016) 1094–1105, https://doi.org/10.1039/c5cy00929d.
[30] D. Chen, Q. Hao, Z. Wang, H. Ding, Y. Zhu, Influence of phase structure and morphology on the photocatalytic activity of bismuth molybdates, CrystEngComm 18 (2016) 1976–1986, https://doi.org/10.1039/c6ce00264a.
[31] J.O.D. Malafatti, A.J. Moreira, C.R. Sciena, T.E.M. Silva, G.P.G. Freschi, E. C. Pereira, E.C. Paris, Prozac® removal promoted by HAP:Nb2O5 nanoparticles system: by-products, mechanism, and cytotoxicity assessment, J. Environ. Chem. Eng. (2020), 104820, https://doi.org/10.1016/j.jece.2020.104820.
[32] A.J. Moreira, A.C. Borges, B.B. de Souza, L.R. Barbosa, V.R. de Mendonça, C. D. Freschi, G.P.G. Freschi, Microwave discharge electrodeless mercury lamp (Hg-MDEL): an energetic, mechanistic and kinetic approach to the degradation of Prozac®, J. Environ. Chem. Eng. 7 (2019), 102916 https://doi.org/10.1016/j.jece.2019.102916.
[33] A.J. Moreira, L.O. Campos, C.P. Maldi, J.A. Dias, E.C. Paris, T.R. Giraldi, G.P. G. Freschi, Photocatalytic degradation of Prozac® mediated by TiO2 nanoparticles obtained via three synthesis methods: sonochemical, microwave hydrothermal, and polymeric precursor, Environ. Sci. Pollut. Res. 27 (2020) 27032–27047, https://doi.org/10.1007/s11356-020-08798-x.
[34] L. Vivas, G.E. Delgado, P. Leret, J.F. Fernández, J.L. Costa-Krämer, P. Silva, Electron paramagnetic resonance study of hopping in CCTO mixed with TiO2, J. Alloy. Compd. 692 (2017) 212–218, https://doi.org/10.1016/J.JALLCOM.2016.09.034.
[35] T. Mashimo, R. Bagum, Y. Ogata, M. Tokuda, M. Okube, K. Sugiyama, Y. Kinemuchi, H. Isobe, A. Yoshiasa, Structure of single-crystal rutile (TiO2) prepared by high-temperature ultracentrifugation, Cryst. Growth Des. 17 (2017) 1460–1464, https://doi.org/10.1021/acs.cgd.6b01818.
[36] M. Gajhede, S. Larsen, S. Rettrup, Electron density of orthoboric acid determined by X-ray diffraction at 105 K and ab initio calculations, Acta Crystallogr. Sect. B Struct. Sci. 42 (1986) 545–552, https://doi.org/10.1107/S0108768186097720.
[37] R.D. Shannon, Revised effective ionic radii and systematic studies of interatomic distances in halides and chalcogenides, Acta Crystallogr. Sect. A 32 (1976) 751–767, https://doi.org/10.1107/S0567739476001551.
[38] S.A. Ansari, M.M. Khan, M.O. Ansari, M.H. Cho, Nitrogen-doped titanium dioxide (N-doped TiO2) for visible light photocatalysis, N. J. Chem. 40 (2016) 3000–3009, https://doi.org/10.1039/C5NJ03478G.
[39] C.F. Macrae, I. Sovago, S.J. Cottrell, P.T.A. Galek, P. McCabe, E. Pidcock, M. Platings, G.P. Shields, J.S. Stevens, M. Towler, P.A. Wood, Mercury 4.0: from visualization to analysis, design and prediction, J. Appl. Crystallogr 53 (2020) 226–235, https://doi.org/10.1107/S1600576719014092.
[40] J.A. Dias, A.L.F. Freire, I. Girotto, C. Del Roveri, V.R. Mastelaro, E.C. Paris, T. R. Giraldi, Phase evolution and optical properties of nanometric Mn-doped TiO2 pigments, Mater. Today Commun. 27 (2021), 102295, https://doi.org/10.1016/j.mtcomm.2021.102295.
[41] R. Maillard, D. Sethio, H. Hagemann, L.M.L.M. Lawson Daku, Accurate computational thermodynamics using anharmonic density functional theory calculations: the case study of B–H species, ACS Omega 4 (2019) 8786–8794, https://doi.org/10.1021/acsomega.9b00218.
[42] N.S. Allen, N. Mahdjoub, V. Vishnyakov, P.J. Kelly, R.J. Kriek, The effect of crystalline phase (anatase, brookite and rutile) and size on the photocatalytic activity of calcined polymorphic titanium dioxide (TiO 2, Polym. Degrad. Stab. 150 (2018) 31–36, https://doi.org/10.1016/j.polymdegradstab.2018.02.008.
[43] T.A. Kandiel, L. Robben, A. Alkaim, D. Bahnemann, Brookite versus anatase TiO 2 photocatalysts: phase transformations and photocatalytic activities, Photochem. Photobiol. Sci. 12 (2013) 602–609, https://doi.org/10.1039/C2PP25217A.
[44] N. Feng, F. Liu, M. Huang, A. Zheng, Q. Wang, T. Chen, G. Cao, J. Xu, J. Fan, F. Deng, Unravelling the efficient photocatalytic activity of boron-induced Ti3+ species in the surface layer of TiO2, Sci. Rep. 6 (2016) 1–9, https://doi.org/10.1038/srep34765.
[45] C. Belver, C. Han, J.J. Rodriguez, D.D. Dionysiou, Innovative W-doped titanium dioxide anchored on clay for photocatalytic removal of atrazine, Catal. Today 280 (2017) 21–28, https://doi.org/10.1016/j.cattod.2016.04.029.
[46] C. Fu, S. Weng, J. Fan, Y. Zhang, Y. Guo, W. Hao, Boron-based materials modified on the surface of TiO2 nanorods via electroless plating toward high-efficient solar-driven water splitting, Chem. Eng. J. 430 (2022), 132881, https://doi.org/10.1016/j.cej.2021.132881.
[47] G. Dong, X. Wang, Z. Chen, Z. Lu, Enhanced photocatalytic activity of vacuum-activated TiO 2 induced by oxygen vacancies, Photochem. Photobiol. 94 (2018) 472–483, https://doi.org/10.1111/php.12874.
[48] S. Jain, J. Shah, N.S. Negi, C. Sharma, R.K. Kotnala, Significance of interface barrier at electrode of hematite hydroelectric cell for generating ecopower by water splitting, Int. J. Energy Res. 43 (2019) 4743–4755, https://doi.org/10.1002/er.4613.
[49] Y. Qu, S. Zhu, X. Dong, H. Huang, M. Qi, Nitrogen-doped TiO2 nanotube anode enabling improvement of electronic conductivity for fast and long-term sodium storage, J. Alloy. Compd. 889 (2021), 161612, https://doi.org/10.1016/j.jallcom.2021.161612.
[50] S.A. Bakar, C. Ribeiro, Low temperature synthesis of N-doped TiO 2 with rice-like morphology through peroxo assisted hydrothermal route: materials characterization and photocatalytic properties, Appl. Surf. Sci. 377 (2016) 121–133, https://doi.org/10.1016/j.apsusc.2016.03.137.
[51] Y. Gong, Y. Yu, H. Kang, X. Chen, H. Liu, Y. Zhang, Y. Sun, H. Song, Synthesis and characterization of graphene oxide/chitosan composite aerogels with high mechanical performance, Polymers 11 (2019) 777, https://doi.org/10.3390/polym11050777.
[52] B. Wu, X. Jiang, S. Yu, P. Bai, X. Guo, J. Lyu, Unveiling the nature of boric acid adsorption by metal-organic frameworks with hexanuclear clusters, Chem. Eng. J. 433 (2022), https://doi.org/10.1016/j.cej.2021.133543.
[53] M. Gałyńska, P. Persson, Emerging polymorphism in nanostructured TiO 2: quantum chemical comparison of anatase, rutile, and brookite clusters, Int. J. Quantum Chem. 113 (2013) 2611–2620, https://doi.org/10.1002/qua.24522.
[54] G. Byzynski, C. Ribeiro, E. Longo, Blue to yellow photoluminescence emission and photocatalytic activity of nitrogen doping in TiO 2 powders, Int. J. Photoenergy 2015 (2015) 1–12, https://doi.org/10.1155/2015/831930.
[55] R. Kawakami, Y. Mimoto, S. Yanagiya, A. Shirai, M. Niibe, Y. Nakano, T. Mukai, Photocatalytic activity enhancement of anatase/rutile-mixed phase TiO 2 nanoparticles annealed with low-temperature O 2 plasma, Phys. Status Solidi 218 (2021) 2100536, https://doi.org/10.1002/pssa.202100536.
[56] N.A. Al Saqri, A. Mondal, J.F. Felix, Y.G. Gobato, V.O. Gordo, H. Albalawi, D. Jameel, H. Alghamdi, F. Al Mashary, D. Taylor, M.S. Abd El-sadek, M. Henini, Investigation of defects in indium doped TiO 2 thin films using electrical and optical techniques, J. Alloy. Compd. 698 (2017) 883–891, https://doi.org/10.1016/j.jallcom.2016.12.294.
[57] X. Kong, Y. Xu, Z. Cui, Z. Li, Y. Liang, Z. Gao, S. Zhu, X. Yang, Defect enhances photocatalytic activity of ultrathin TiO2 (B) nanosheets for hydrogen production by plasma engraving method, Appl. Catal. B Environ. 230 (2018) 11–17, https://doi.org/10.1016/j.apcatb.2018.02.019.
[58] K.C. Huang, S.H. Chien, Improved visible-light-driven photocatalytic activity of rutile/titania-nanotube composites prepared by microwave-assisted hydrothermal process, Appl. Catal. B Environ. 140–141 (2013) 283–288, https://doi.org/10.1016/j.apcatb.2013.04.001.
[59] A.E.B. Lima, R.Y.N. Reis, L.S. Ribeiro, L.K. Ribeiro, M. Assis, R.S. Santos, C.H. M. Fernandes, L.S. Cavalcante, E. Longo, J.A.O. Osajima, G.E. Luz, Microwave-assisted hydrothermal synthesis of CuWO4-palygorskite nanocomposite for enhanced visible photocatalytic response, J. Alloy. Compd. 863 (2021), 158731, https://doi.org/10.1016/j.jallcom.2021.158731.
[60] H.-T. Nguyen Thi, K.-N. Tran Thi, N.B. Hoang, B.T. Tran, T.S. Do, C.S. Phung, K.-O. Nguyen Thi, Enhanced degradation of rhodamine B by metallic organic frameworks based on NH2-MIL-125(Ti) under visible light, Materials 14 (2021) 7741, https://doi.org/10.3390/ma14247741.
[61] W. Li, Z. Wang, Y. Li, J.B. Ghasemi, J. Li, G. Zhang, Visible-NIR light-responsive 0D/2D CQDs/Sb2WO6 nanosheets with enhanced photocatalytic degradation performance of RhB: unveiling the dual roles of CQDs and mechanism study, J. Hazard. Mater. 424 (2022), 127595, https://doi.org/10.1016/j.jhazmat.2021.127595.
[62] Y. Gao, F. Liu, X. Chi, Y. Tian, Z. Zhu, R. Guan, J. Song, A mesoporous nanofibrous BiVO4-Ni/AgVO3 Z-scheme heterojunction photocatalyst with enhanced photocatalytic reduction of Cr6+ and degradation of RhB under visible light, Appl. Surf. Sci. 603 (2022), 154416, https://doi.org/10.1016/j.apsusc.2022.154416.
[63] Q. Zhang, Z. Zhang, D. Zhao, L. Wang, H. Li, F. Zhang, Y. Huo, H. Li, Synergistic photocatalytic-photothermal contribution enhanced by recovered Ag+ ions on MXene membrane for organic pollutant removal, Appl. Catal. B Environ. 320 (2023), 122009, https://doi.org/10.1016/j.apcatb.2022.122009.

[64] P.P. Gotipamul, G. Vattikondala, K.D. Rajan, S. Khanna, M. Rathinam, S. Chidambaram, Impact of piezoelectric effect on the heterogeneous visible photocatalysis of g-C3N4/Ag/ZnO tricomponent, Chemosphere 287 (2022), 132298, https://doi.org/10.1016/j.chemosphere.2021.132298.
[65] P. Shao, J. Tian, Z. Zhao, W. Shi, S. Gao, F. Cui, Amorphous TiO2 doped with carbon for visible light photodegradation of rhodamine B and 4-chlorophenol, Appl. Surf. Sci. 324 (2015) 35–43, https://doi.org/10.1016/j.apsusc.2014.10.108.
[66] C. Wu, M. Yin, R. Zhang, Z. Li, Z. Zou, Z. Li, Further studies of photodegradation and photocatalytic hydrogen production over Nafion-coated Pt/P25 sensitized by rhodamine B, Int. J. Hydrog. Energy 45 (2020) 22700–22710, https://doi.org/10.1016/j.ijhydene.2020.06.098.
[67] J.W. Kwon, K.L. Armbrust, Laboratory persistence and fate of fluoxetine in aquatic environments, Environ. Toxicol. Chem. 25 (2006) 2561–2568, https://doi.org/10.1897/05-613R.1.
[68] E.S. Papas, C.N. Chaldezos, J. Atta-Politou, M.A. Koupparis, Construction of a fluoxetine ion chemical sensor and its application for the determination of pKa value of fluoxetine conjugated acid, complexation study with β-cyclodextrin and formulations assay, Anal. Lett. 43 (2010) 2171–2183, https://doi.org/10.1080/00032711003687104.
[69] A.J. Moreira, S.R.R. Padilha, V.R. de Mendonça, E.C. Paris, C. Ribeiro, G.P. G. Freschi, T.R. Giraldi, Photoactivity of TiO2 nanoparticles covered with nitro group in Fluoxetine and Rhodamine-B degradation, Desalin. Water Treat. 205 (2020) 252–263, https://doi.org/10.5004/dwt.2020.26379.